Applied Physics B (2018) 124:65
https://doi.org/10.1007/s00340-018-6938-5

Applied Physics B
Lasers and Optics

Ab-initio determination of porous silicon refractive index confirmed by infrared transmittance measurements of an omnidirectional multilayer reflector

Alessio Palavicini[1] · **Chumin Wang**[1]

Received: 27 May 2017 / Accepted: 27 March 2018 / Published online: 30 March 2018

Abstract
We report a multiscale design of omnidirectional Bragg mirrors based on dielectric multilayers by combining quantum mechanical and electromagnetic theories. This design begins with the calculation of electric permittivity for each layer using the density functional theory, followed by a transfer matrix study of light propagation along the multilayer reflector. The theoretical results were further validated by fabricating free-standing porous silicon multilayer films obtained through electrochemical etching of p^+-type [100]-oriented crystalline Si wafers, alternating two anodic current densities. The measured infrared transmittance spectra confirm the position and width of the photonic bandgap predicted by the multiscale design.

1 Introduction

Mirrors have been the most widely used optical devices and of great importance for the human self-awareness [1]. Besides the conventional silvered-glass reflectors, there are multilayered dielectric ones, which have the advantage of minimizing the absorption losses in comparison with metallic reflectors [2]. For an N-layer Bragg reflector, the transmittance (T) at optical band-gap edges goes to zero as N^{-2}, while at the gap center, T tends exponentially to zero with N [3]. However, the width of this gap is usually limited, which can be overcome by introducing a chirped multilayer structure with variable layer thickness [4, 5]. Hence, an omnidirectional dielectric reflector or anti-reflector that works for all incident angles and a wide range of light frequencies with minimal light absorption would be an ideal component of optical fibers [6] and solar cells [7].

Among the dielectric materials, porous silicon (PSi) is considered as a suitable material for infrared photonic devices, since its dielectric constant depends on the porosity fixed by etching parameters [8]. Such devices can alter the propagation of electromagnetic waves or photons, and at the same time, they can be integrated with current electronic devices based on crystalline silicon (c-Si). A PSi omnidirectional mirror can be achieved through a multilayer structure, such as a Bragg reflector, whose layers are obtained by alternating current densities during the electrochemical etching [9–12].

In this article, we present a new multiscale design approach, in which the dielectric function of each layer is calculated by means of the density functional theory (DFT) and the light reflectance of multilayers is determined through the transfer matrix method (TMM) fed by the DFT results. To validate this approach, we further fabricate PSi multilayer samples and measure their light transmittance in the infrared range.

2 Multiscale design

Nowadays, DFT is the most used ab-initio method to calculate electronic and structural properties of molecules and solids. The PSi optical properties can be predicted using the supercell technique within DFT, through a double self-consistent procedure: one for the electronic density distribution and another for the geometrical optimization to determine the atomic positions of minimal energy. However, this procedure requires an excessive amount of computing effort, since millions of atoms should be explicitly considered for determining the optical behavior of a PSi multilayer device with thickness of 10 microns and 50% of porosity. Alternatively, we propose a combination of DFT and TMM. In the

✉ Chumin Wang
chumin@unam.mx

[1] Instituto de Investigaciones en Materiales, Universidad Nacional Autónoma de México, Mexico City, Mexico

former, the supercell technique is used to model ordered silicon pores, whereas in the latter, both phase shifts due to the layer interface and the propagation of electromagnetic wave along each layer are considered.

To determine the dependence of PSi dielectric function on porosity, we use a supercell of 32 Si atoms, in which 5, 9, 13, and 18 of them were removed and the dangling bonds were saturated with hydrogen atoms to model freshly-etched samples, producing columnar hydrogen-passivated pores with porosities of 15.6, 28.1, 40.6, and 52.25%, respectively, as shown in Fig. 1a–d. The DFT calculations were carried out using the CASTEP code [13] within the Biovia Materials Studio in which the same parameters of Ref [14]. were used. The resulting real (red open circles) and imaginary (blue lines) parts of the dielectric function (ε) are presented in Fig. 1a–d for each analyzed structure illustrated by insets.

In Fig. 1e, the static dielectric constants (red circles) obtained from the calculated dielectric functions at zero wavenumber are plotted versus porosity, which is defined as $1 - M_{\mathrm{PSi}}/M_{\mathrm{cSi}}$ being M_{PSi} and M_{cSi}, respectively, the supercell atomic masses of PSi and c-Si. These ab-initio results are compared with those $\bar{\varepsilon}$ obtained from the Bruggeman effective medium model given by [15]:

$$0 = f\frac{\varepsilon_1 - \bar{\varepsilon}}{\varepsilon_1 + 2\bar{\varepsilon}} + (1-f)\frac{\varepsilon_2 - \bar{\varepsilon}}{\varepsilon_2 + 2\bar{\varepsilon}}, \tag{1}$$

where $\bar{\varepsilon}$ is the resulting dielectric constant of effective medium, and ε_1 and ε_2 are the static dielectric constants for two types of spherical inclusions with filling factor f and $1-f$, respectively. For our case, component 1 is the air with $\varepsilon_1 = 1$, component 2 is c-Si with $\varepsilon_2 \approx 11.94$, and the porosity is considered equal to the air-filling factor f of the sample. Observe the remarkable coincidence between the ab-initio and effective medium results, since neither the pore morphology nor its distribution is relevant for the static case with infinite wavelength.

We further calculate the light propagation in dielectric multilayers using the TMM [16]. The incident ($\mathbf{E}_n^{(1)}$) reflected ($\mathbf{E}_n^{(2)}$) and transmitted ($\mathbf{E}_{n+1}^{(1)}$) electric field amplitudes of plane waves with respective wavevectors $\mathbf{K}_n^{(1)}$, $\mathbf{K}_n^{(2)}$, and $\mathbf{K}_{n+1}^{(1)}$ near the interface between layers n and $n+1$ are illustrated in Fig. 2. In layer n, the electric field at position $\mathbf{r}$ and time t can be expressed by

$$\mathbf{E}_n(\mathbf{r},t) = \mathbf{E}_n^{(1)} e^{i\left[\mathbf{K}_n^{(1)}\cdot\mathbf{r}-\omega t\right]} + \mathbf{E}_n^{(2)} e^{i\left[\mathbf{K}_n^{(2)}\cdot\mathbf{r}+\omega t\right]}. \tag{2}$$

The propagation of a transverse electric (TE) or transverse magnetic (TM) polarized wave across the interface between non-magnetic dielectric layers $n-1$ and n, denoted as $n|n-1$, can be described by

$$\begin{pmatrix} E_{n,U}^{+} \\ E_{n,U}^{-} \end{pmatrix} = T_{n|n-1}\begin{pmatrix} E_{n-1,L}^{+} \\ E_{n-1,L}^{-} \end{pmatrix} = \begin{pmatrix} 1 & 0 \\ 0 & q\frac{\cos\theta_{n-1}}{\cos\theta_n} \end{pmatrix}\begin{pmatrix} E_{n-1,L}^{+} \\ E_{n-1,L}^{-} \end{pmatrix}, \tag{3}$$

where the refractive index of layer n is denoted by η_n, $q = \eta_{n-1}/\eta_n$ for TE or $q = \eta_n/\eta_{n-1}$ for TM [16, 17], and

$$\begin{cases} E_{n,S}^{+} \equiv E_{n,S}^{(1)} + E_{n,S}^{(2)} \\ E_{n,S}^{-} \equiv -i\left(E_{n,S}^{(1)} - E_{n,S}^{(2)}\right) \end{cases}, \tag{4}$$

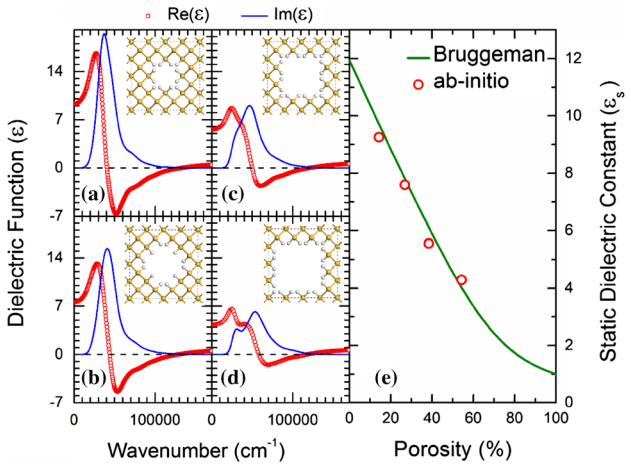

Fig. 1 **a**–**d** Real (red circles) and imaginary (blue lines) parts of the dielectric functions (ε) of PSi, whose supercell structures (dashed lines) are shown in the insets, where silicon (large yellow spheres) pores are passivated by hydrogen atoms (small white spheres). **e** Static dielectric constants (red circles) obtained from **a** to **d** as functions of the porosity are compared with those derived from the Bruggeman effective medium model (green line)

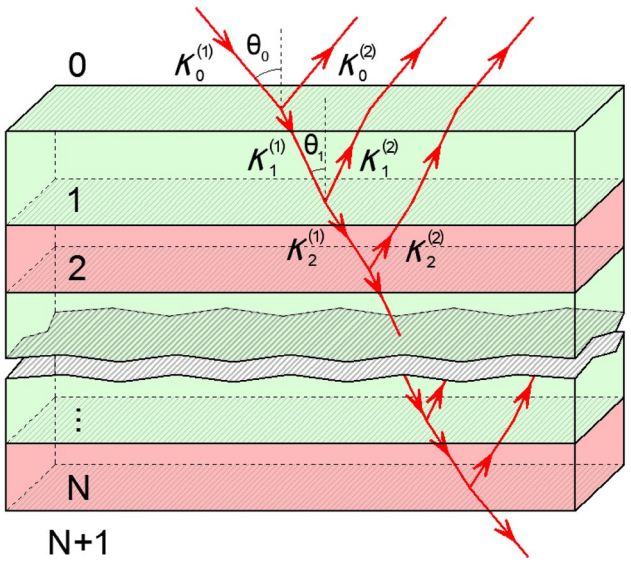

Fig. 2 Light propagation (red arrows) in N dielectric layers, whose incidence angle (θ_n) as well as wave vectors of the incident ($\mathbf{K}_n^{(1)}$) and reflected ($\mathbf{K}_n^{(2)}$) light rays in layer n are drawn

being $S = U$ or L for electric fields evaluated at the upper or lower face of layer n. Moreover, the wave propagation through layer n of thickness d_n with wavelength λ produces a phase change ϕ_n; in other words, $E^{(1)}_{n,L} = E^{(1)}_{n,U} e^{i\phi_n}$ and $E^{(2)}_{n,L} = E^{(2)}_{n,U} e^{-i\phi_n}$. Such phase change is [16]

$$\phi_n = \frac{2\pi \eta_n d_n \cos\theta_n}{\lambda}. \tag{5}$$

Thus

$$\begin{pmatrix} E^+_{n,L} \\ E^-_{n,L} \end{pmatrix} = T_n \begin{pmatrix} E^+_{n,U} \\ E^-_{n,U} \end{pmatrix} = \begin{pmatrix} \cos\phi_n & -\sin\phi_n \\ \sin\phi_n & \cos\phi_n \end{pmatrix} \begin{pmatrix} E^+_{n,U} \\ E^-_{n,U} \end{pmatrix}. \tag{6}$$

Leading to an entire transfer matrix (M) of N layers given by

$$\begin{pmatrix} E^+_{N+1,U} \\ E^-_{N+1,U} \end{pmatrix} = M \begin{pmatrix} E^+_{0,L} \\ E^-_{0,L} \end{pmatrix} = T_{N+1|N} \left(\prod_{n=1}^{N} T_n T_{n|n-1} \right) \begin{pmatrix} E^+_{0,L} \\ E^-_{0,L} \end{pmatrix}. \tag{7}$$

Finally, we can calculate the transmittance (T) and reflectance (R) of the multilayer using

$$\begin{cases} T = \left| \frac{E^{(1)}_{N+1,U}}{E^{(1)}_{0,L}} \right|^2 = \frac{4}{(m_{11}+m_{22})^2 + (m_{12}-m_{21})^2} \\ R = \left| \frac{E^{(2)}_{0,L}}{E^{(1)}_{0,L}} \right|^2 = \frac{(m_{11}-m_{22})^2 + (m_{12}+m_{21})^2}{(m_{11}+m_{22})^2 + (m_{12}-m_{21})^2} \end{cases}, \tag{8}$$

where m_{ij} are the matrix elements of the entire transfer matrix M.

Equation (8) allows us to calculate the reflection and transmission spectra of whole multilayer structures. Figure 3a–f shows the reflectance spectra of periodic binary dielectric heterostructures with 10, 12,…, 20 layers ordered following an ABAB…AB periodic pattern, where the refractive index and thickness of layers type A (B) are 1.57 (2.13) and 239 nm (176 nm), respectively. These parameters were chosen to satisfy the quarter-wave condition derived from Eq. (5) and given by $\eta_A d_A = \eta_B d_B = \lambda_0/4$ for both types of layers, arising from a high-reflectance band centered at $\lambda_0 = 1500$ nm, or equivalently a wavenumber of 6666.67 cm^{-1}. Note in these figures, the well-defined high-reflectance band when the number of layers increases.

Figure 4 shows the reflectance spectra of 20-layer periodic binary heterostructures, whose refractive indexes (porosity) of layers type A and B are (a) 1.83 (60%) and 2.43 (40%), (b) 1.56 (70%) and 2.71 (30%), (c) 1.32 (80%) and 2.97 (20%), and (d) 1.14 (90%) and 3.22 (10%), respectively. These refractive indexes were determined from the corresponding porosities through the Bruggeman effective medium theory and the layer thicknesses were chosen to satisfy the quarter-wave condition for a wavelength of 1500 nm. Observe the widening of high-reflectance band as the refractive index contrast ($\eta_B - \eta_A$) grows. Nevertheless, to integrate optical heterostructures into current electronic devices, the contrast would be limited by the dielectric constant of c-Si. An alternative way to achieve a wide photonic bandgap could be the stacking of multilayer groups, as analyzed in Fig. 5.

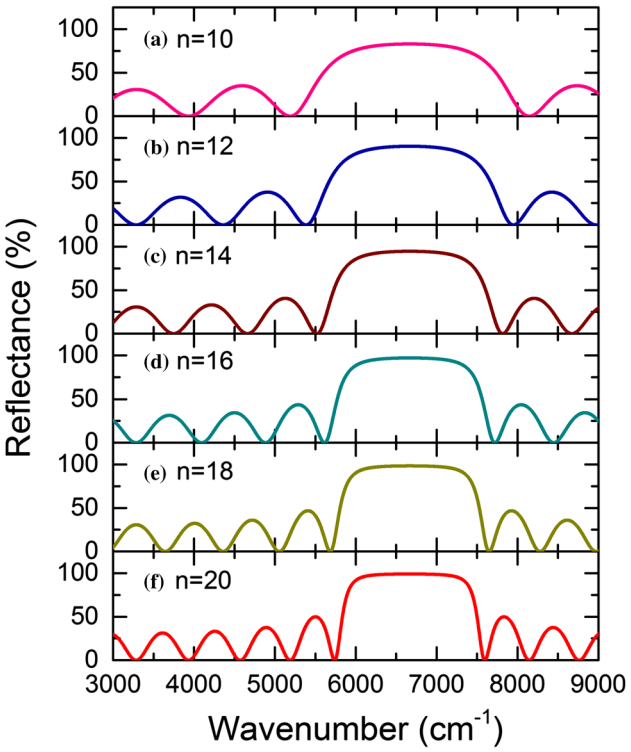

Fig. 3 **a–f** Calculated reflectance spectra of n-layer periodic dielectric heterostructures obtained by alternating layers type A with refractive index of 1.57 and type B of 2.13

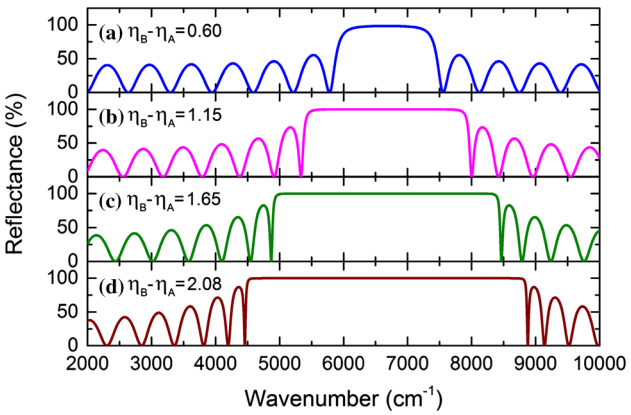

Fig. 4 Calculated reflectance spectra of 20-layer periodic binary dielectric structures, whose layers A and B have refractive indexes of **a** 1.83 and 2.43, **b** 1.56 and 2.71, **c** 1.32 and 2.97, and **d** 1.14 and 3.22, respectively

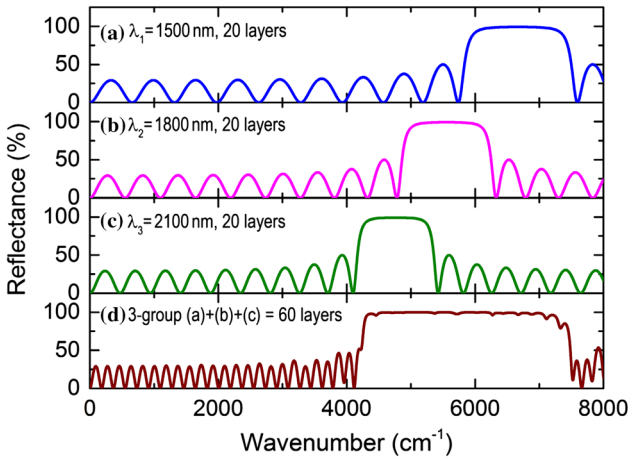

Fig. 5 Calculated reflectance spectra of 20-layer periodic binary dielectric heterostructures with central wavenumber of **a** 6666.7 cm^{-1}, **b** 5555.6 cm^{-1}, and **c** 4761.9 cm^{-1}, while **d** corresponds to a multilayer obtained by stacking the three previous ones, having a total of 60 layers

Figure 5a shows the reflectance spectrum of a 20-layer periodic binary dielectric heterostructure with refractive indexes of $\eta_A = 1.57$ ($\eta_B = 2.13$) and thicknesses of $d_{1A} = 239.0$ nm ($d_{1B} = 175.8$ nm) for a central wavelength of $\lambda_1 = 1500$ nm or 6666.7 cm^{-1}. Analogously, Fig. 5b, c illustrates the reflectance spectra of 20-layer binary heterostructures with the same refractive indexes, as shown in Fig. 5a, but thicknesses $d_{2A} = 286.9$ nm ($d_{2B} = 211.0$ nm) for $\lambda_2 = 1800$ nm, or 5555.6 cm^{-1}, and $d_{3A} = 334.7$ nm ($d_{3B} = 246.2$ nm) for $\lambda_3 = 2100$ nm or 4761.9 cm^{-1}, respectively.

The photonic bandgaps of Fig. 5a–c cover the intervals (6145, 7188 cm^{-1}), (5121, 5990 cm^{-1}), and (4389, 5135 cm^{-1}) with 97% reflectance, respectively. Hence, if we stack these three 20-layer heterostructures, the resulting high-reflectance band would cover the interval from 4389 to 7188 cm^{-1}. Figure 5d shows the reflectance spectrum obtained from stacking the three multilayers of 5a–c. Notice that the width of resulting high-reflectance band is roughly the sum of individual ones obtained from each multilayer prior to stacking.

Based on this widening of the high-reflection band through the stacking of narrow-band mirrors, we set the task of designing a structure consisting of seven stacked groups of multilayers to obtain a wide high-reflectance band using a minimal number of layers. From Fig. 5, we observe that groups with larger central wavelength (smaller wavenumber) have more compressed reflectance spectra, and then, we need less layers in such groups to obtain the same squareness in the high-reflectance band. The layer parameters of this design for each group are summarized in Table 1 and its reflectance as a function of incidence angle and wavenumber is shown in Fig. 6a–c using color scale respectively for TE, TM, and unpolarized modes.

The unpolarized reflectance spectrum was obtained from the algebraic average of TE and TM ones [18]. Observe that the width of high-reflectance (> 90%) band for TE increases with the incidence angle (θ_0) and such band covers the interval from 3400 to 7100 cm^{-1} for all θ_0. In contrast, the TM mode possesses reflectance dips in the high-reflectance band for incidence angles larger than 40° and around the Brewster's angle of 61.6°, which can be obtained from the average refractive index of the multilayer. Such Brewster's angle is shown as a red zone in Fig. 6b for low wavenumbers. Note also the oscillating behavior of transmittance outside of the band, giving rise to the red stripes corresponding to almost perfect transmission zones.

3 Experimental validation

The multilayer structure designed in the previous section served as a guide for the fabrication of a binary PSi multilayer obtained from <100>-oriented, boron-doped c-Si Motorola wafers with an electrical resistivity of 0.01–0.03 Ω cm submerged in an electrolyte composed of 48.0–51.0% hydrofluoric acid (HF) and ethyl alcohol absolute anhydrous (EtOH), both from JT Baker, in a 1:2 volumetric ratio. Its high- and low-porosity layers were obtained by applying respectively a high and low anodizing electrical current over a circular etching area of 2.45 cm^2. The etching process using an Agilent 6645 A current source was controlled by computer and carried out in an electrochemical cell

Table 1 Parameters for the designed seven-group stacked multilayer

Group	1		2		3		4		5		6		7	
λ_0 (nm)	1500		1800		2100		2400		2700		3000		3300	
Type	A	B	A	B	A	B	A	B	A	B	A	B	A	B
Number of Layers	10	10	9	9	8	8	7	7	6	6	5	5	4	4
Refractive index	1.57	2.13	1.57	2.13	1.57	2.13	1.57	2.13	1.57	2.13	1.57	2.13	1.57	2.13
Thickness (nm)	239.0	175.8	286.9	211.0	334.7	246.2	382.5	281.4	430.3	316.5	478.1	351.7	525.9	386.9

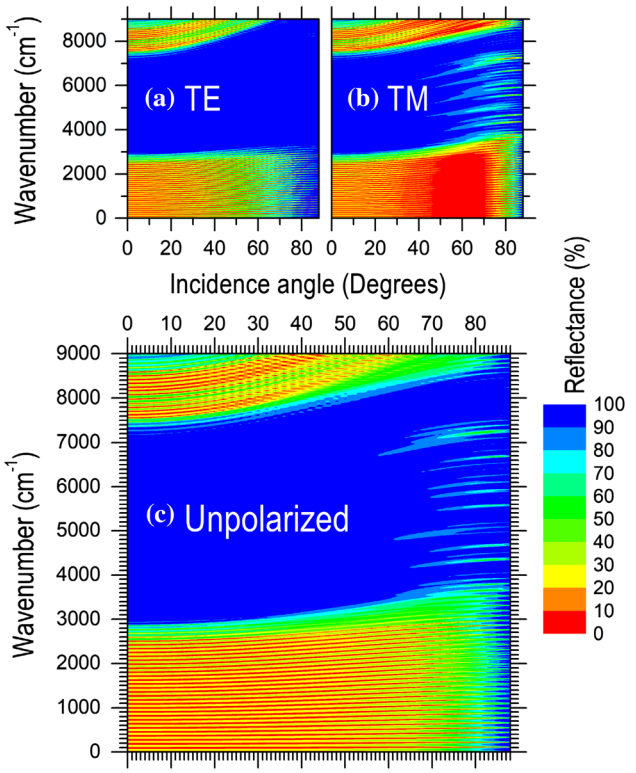

Fig. 6 Calculated **a** TE, **b** TM, and **c** unpolarized reflectance spectra in color scale versus incidence angle and wavenumber for an omnidirectional mirror consisting of a seven-group multilayer, where each group has a high-reflectance band centered at its λ_0, as given in Table 1

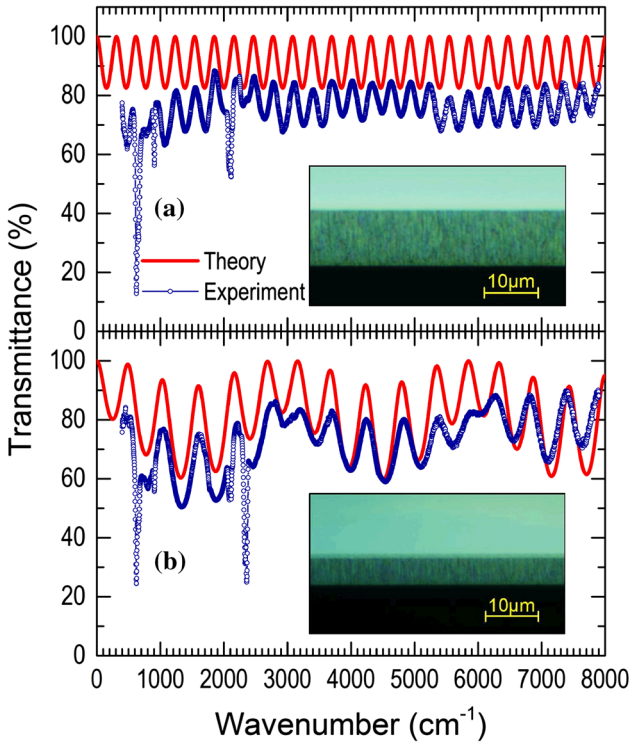

Fig. 7 Calculated (red lines) and measured (blue open circles) transmittance spectra for **a** single and **b** double PSi layers, whose thicknesses were acquired from optical microscope images as shown in the respective insets

described in Ref. [19], which consists of a c-Si wafer with a sputtered gold coating on the backside acting as anode and a platinum cathode immersed into the electrolyte, which was recirculated by a peristaltic pump at a rate of 100 mL/min, to remove gas bubbles generated by the electrochemical reaction. To obtain free-standing PSi films, at the end of the etching process an electropolishing current of 1100 mA for 5 s was applied to detach the multilayer from the c-Si substrate [20].

It has been noted in the previous section that the refractive index contrast of layers is fundamental to obtain a wide high reflective band. However, this contrast has experimental limitations, such as the poor mechanical strength of high-porosity PSi layers and electrolyte flow blockage of low-porosity layers. For this study, we chose the high- and low-porosity PSi layers produced by applying respectively DC currents of 150 and 10 mA during the anodization. Each type of layer was individually characterized by fabricating a freestanding sample and another with substrate using the same etching parameters. The first two samples with substrate were used to determine the layer thickness by cleaving them and photographing the side view of the cleaved edge, as shown in the insets of Fig. 7. The other two free-standing samples were mounted to a thin film holder with a central aperture to measure their infrared transmittance by using a Shimadzu IRAffinity-1 Fourier transform infrared (FTIR) spectrophotometer. The transmittance spectra were obtained from an average of 20 scans with a resolution of 0.5 cm^{-1}, using the Happ–Genzel apodization function and having subtracted the background scan. The measured FTIR spectrum (blue open circles) of a monolayer produced from 150 mA applied for 200 s, giving a layer thickness of 10.4 μm is shown in Fig. 7a, while the spectrum (blue open circles) of a double layer obtained from the application of 150 mA for 96 s followed by 10 mA for 120 s, respectively, yielding 5 and 0.8 μm, is illustrated in Fig. 7b. This double layer is used, since the low-porosity layer of 10 mA hinders the flow of electrolyte as its thickness increases and a thin (< 1 μm)-isolated low-porosity free-standing layer is difficult to manipulate. The calculated transmittance spectra (red lines) are also shown in Fig. 7a for the monolayer and 7b for the double layer, in which porosities of 69.5 and 50% were used for the high- and low-porosity layers, respectively.

In Fig. 7, the mismatch between the theoretical and experimental transmittance spectra is mainly related to the absence of IR absorption due to structural disorder in PSi samples, which is not considered in the modelling. However,

there are several identifiable absorption peaks located at 626, 908, 2114, and 2359 cm^{-1}. The first three can, respectively, be attributed to Si–H bending, Si–H_2 scissor bending, and Si–H_2 asymmetric stretching vibrational modes [21], while the last one is the main absorption peak of carbon dioxide present in the air [22].

To validate the design of Sect. 2, PSi multilayer samples made with seven stacked groups were fabricated by alternating the studied electrical currents with different application times, as specified in Table 2, following the three-group realization of Ref. [23]. The etching times were established based on the monolayer and double layer measurements of Fig. 2, while the thickness of each layer was calculated assuming constant etch rates and confirmed by the scanning electron microscopy (SEM) image presented in inset (a) of Fig. 8. As done with the single- and double-layered samples of Fig. 7, two seven-group heterostructures were synthesized using the same etching parameters. One of them was used to determine its morphology through SEM imaging, as seen in the insets of Fig. 8, where (a) is the side view of its cleaved edge and (b) is the top view of the sample. Observe the flatness of interfaces between high- and low-porosity layers in inset (a) due to electrolyte recirculation, and the sponge-like Si skeleton seen as brighter areas, whereas the pores as dark spots in inset (b). The other seven-group sample was separated from c-Si substrate to measure its transmittance by means of FTIR spectroscopy for normal incidence and compared with the corresponding calculated prediction, as shown by the red line in Fig. 8. Notice that the predicted photonic bandgap from 3000 to 7200 cm^{-1}, defined for a reflectance higher than 90% for unpolarized light with incidence angles up to 57°, as shown in Fig. 6c.

The measured infrared transmittance spectrum of Fig. 8 seems to confirm the calculated band-gap width as well as the oscillating behavior at low wavenumbers. Conversely, the experimental transmittance band edge at high wavenumbers is less defined. This fact could be originated from a gradient of porosity in the multilayer sample, due to the variation of etching effectiveness with depth producing the highly-branched pores of Fig. 8c, in contrast to the columnar pores in the lower layers, as shown in Fig. 8d. The green squares in Fig. 8 show the calculated transmittance obtained

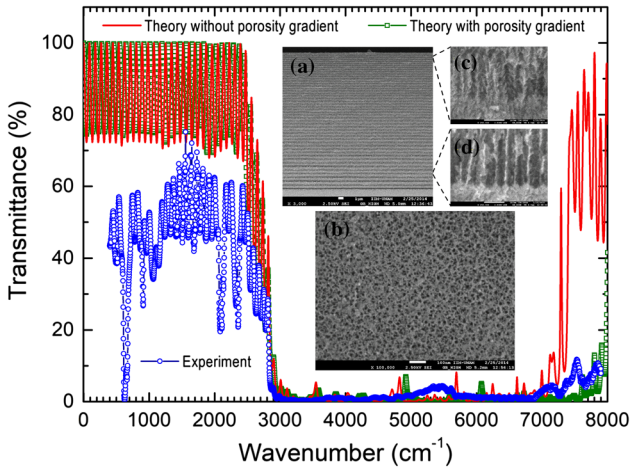

Fig. 8 Calculated infrared transmittance spectra of the seven-group multilayer, with (green squares) and without (red line) porosity gradient, compared with experiment (blue circles). Insets: SEM images of **a** cross section, **b** top view, and **c**–**d** magnifications of the seven-group PSi multilayer sample

with the same parameters as the red line spectrum of this figure but including a 10% decreasing porosity gradient from top to bottom.

In addition, the reflector's omnidirectionality was studied by rotating the sample holder in the FTIR spectrophotometer from normal incidence to angles of 10°, 20°, 30°, 40°, 45°, and 50°, and the measured (red lines) transmittance spectra in comparison with the calculated (dark cyan dots) ones are shown in Fig. 9. The calculated infrared transmittance spectra were obtained using the parameters of Table 2 and a porosity gradient of 10%, as shown in Fig. 8. Observe that the high-reflectance band shifts and extends towards higher wavenumbers as the incidence angle increases, in accordance with the theoretical results.

4 Conclusions

The creation of new materials from ab-initio design constitutes one of the greatest dreams for generations of scientists. Nowadays, even with the exponential growth of modern

Table 2 Etching parameters for the PSi seven-group stacked multilayer

Group	1		2		3		4		5		6		7	
Type	A	B	A	B	A	B	A	B	A	B	A	B	A	B
Number of layers	10	10	9	9	8	8	7	7	6	6	5	5	4	4
Current (mA)	150	10	150	10	150	10	150	10	150	10	150	10	150	10
Time (s)	5	25	6	30	7	35	8	40	9	45	10	50	11	55
Porosity (%)	69.5	50	69.5	50	69.5	50	69.5	50	69.5	50	69.5	50	69.5	50
Refractive index	1.57	2.13	1.57	2.13	1.57	2.13	1.57	2.13	1.57	2.13	1.57	2.13	1.57	2.13
Thickness (nm)	260	167	312	200	364	233	416	267	468	300	520	333	572	367

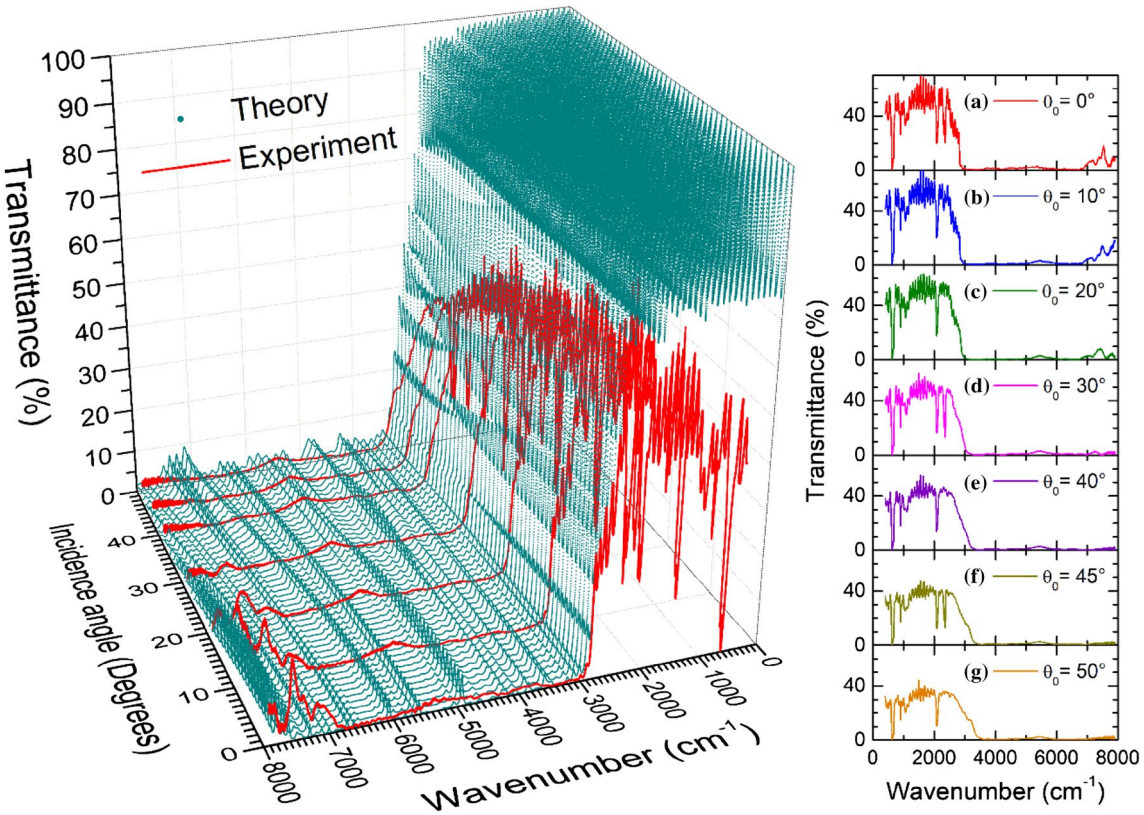

Fig. 9 Left: measured (red lines) infrared transmittance spectra of the seven-group multilayer sample in comparison with calculated (dark cyan dots) ones using the parameters of Table 2 and a porosity gradient of 10%. Right: the same measured spectra of left panel in 2D form for incidence angles (θ_0) of 0°, 10°, 20°, 30°, 40°, 45°, and 50°

computing capability predicted by Moore's law, the macroscopic material architecture at atomic scale calculations seems to be practically unachievable for the next 50 years if the ab-initio computing time grows linearly with the system size. Thus, the multiscale design of bulk materials and devices starting from first-principles calculations could be a feasible approach, as done in this work.

Among the results, we would remark, despite the simplicity of this multiscale approach, the agreement of theory and experiment on the location of the low-wavenumber edge of the photonic bandgap, although the high-wavenumber edge could not be analyzed in this work. In addition, the presented multigroup design with a non-uniform number of elements for each group produces a wide reflective band with a small number of layers for incidence angles of up to 50°, and this design was confirmed by the samples made from PSi. Moreover, there is an outstanding coincidence between the static dielectric constants obtained from the Bruggeman effective medium theory and from the ordered-pore DFT. This coincidence happens when the wavelengths are much longer than the pore size, as it occurs in IR experiments. In contrast, for UV and visible region studies, it is necessary to use the full wavelength-dependent dielectric function obtained from DFT calculations, including its imaginary part. Finally, this multiscale design method based on ab-initio calculations can be used for the study of other optical devices, such as cavities [24] and filters [25].

Acknowledgements We would like to thank Omar Novelo and Yolanda Flores for their technical assistance. This work has been partially supported by UNAM-IN106317 and CONACyT-252943. Computations were performed at Miztli of DGTIC, UNAM.

References

1. M. Anderson (ed.), *The Book of the Mirror. An Interdisciplinary Collection Exploring the Cultural Story of the Mirror* (Cambridge Scholars Publishing, Newcastle upon Tyne, 2007)
2. Y. Fink, J.N. Winn, S. Fan, C. Chen, J. Michel, J.D. Joannopoulos, E.L. Thomas, A dielectric omnidirectional reflector. Science **282**, 1679 (1998)
3. J. Lekner, Light in periodically stratified media. J. Opt. Soc. Am. A **11**, 2892 (1994)
4. R. Szipocs, K. Ferencz, C. Spielmann, F. Krausz, Chirped multilayer coatings for broadband dispersion control in femtosecond lasers. Opt. Lett. **19**, 201 (1994)

5. E. Xifré-Pérez, L.F. Marsal, J. Pallarès, J. Ferré-Borrull, Porous silicon mirrors with enlarged omnidirectional band gap. J. Appl. Phys. **97**, 064503 (2005)
6. M. Ibanescu, S.G. Johnson, M. Soljacic, J.D. Joannopoulos, Y. Fink, O. Weisberg, T.D. Engeness, S.A. Jacobs, M. Skorobogatiy, Analysis of mode structure in hollow dielectric waveguide fibers. Phys. Rev. E **67**, 046608 (2003)
7. Y. Yao, K.-T. Lee, X. Sheng, N.A. Batara, N. Hong, J. He, L. Xu, M.M. Hussain, H.A. Atwater, N.S. Lewis, R.G. Nuzzo, J.A. Rogers, Porous nanomaterials for ultrabroadband omnidirectional anti-reflection surfaces with applications in high concentration photovoltaics. Adv. Energy Mater. **7**, 1601992 (2017)
8. L. Canham (ed.), *Handbook of Porous Silicon* (Springer, Zug, 2014)
9. J.E. Lugo, H.A. Lopez, S. Chan, P.M. Fauchet, Porous silicon multilayer structures. A photonic band gap analysis. J. Appl. Phys. **91**, 4966 (2002)
10. E. Xifré-Pérez, L.F. Marsal, J. Ferré-Borrull, J. Pallarès, Porous silicon omnidirectional mirrors and distributed Bragg reflectors for planar waveguide applications. J. Appl. Phys. **102**, 063111 (2007)
11. D. Ariza-Flores, L.M. Gaggero-Sager, V. Agarwal, Study of the omnidirectional photonic bandgap for dielectric mirrors based on porous silicon: effect of optical and physical thickness. Nanoscale Res. Lett. **7**, 391 (2012)
12. D. Estrada-Wiese, J.A. del Río, R. Nava, J. Gómez-Ocampo, J. Tagüeña-Martínez, Z. Montiel-González, Staggered Padé wavelength distribution for multi-Bragg photonic mirrors. Solar Energy Mater. Solar Cells **141**, 315 (2015)
13. M.D. Segall, P.J.D. Lindan, M.J. Probert, C.J. Pickcard, P.J. Hasnip, S.J. Clark, M.C. Payne, First-principles simulation: ideas, illustrations and the CASTEP code. J. Phys. Condens. Matter. **14**, 2717 (2002)
14. Y. Bonder, C. Wang, A first-principles model of birefringent porous silicon. J. Appl. Phys. **100**, 044319 (2006)
15. T.C. Choy, *Effective Medium Theory. Principles and Applications*. (Oxford University Press, New York, 1999)
16. P. Yeh, *Optical Waves in Layered Media* (Wiley, New Jersey, 2005), p. 102
17. J.J. Saarinen, S.M. Weiss, P.M. Fauchet, J.E. Sipe, Reflectance analysis of a multilayer one-dimensional porous silicon structure: theory and experiment. J. Appl. Phys. **104**, 013103 (2008)
18. S. Chandrasekhar, *Radiative Transfer* (Dover Pub. Inc., New York, 1960), p. 30
19. R. Cisneros, C. Ramírez, C. Wang, Ellipsometry and ab initio approaches to the refractive index of porous silicon. J. Phys. Condens. Matter. **19**, 395010 (2007)
20. P. Alfaro, A. Palavicini, C. Wang, Hydrogen: oxygen and hydroxyl on porous silicon surface: a joint density-functional perturbation theory and infrared spectroscopy approach. Thin Solid Films **571**, 206 (2014)
21. Y.H. Ogata in *Handbook of Porous Silicon*, ed. by L. Canham (Springer, Zug, 2014), p. 473
22. B.C. Smith, *Fundamentals of Fourier Transform Infrared Spectroscopy*, 2nd edn. (CRC Press, Florida, 2011), p. 12
23. E. Xifré-Pérez, L.F. Marsal, J. Ferré-Borrull, J. Pallarès, Low refractive index contrast porous silicon omnidirectional reflectors. Appl. Phys. B **95**, 169 (2009)
24. M. Song, P. Belov, P. Kapitanova, Wireless power transfer inspired by the modern trends in electromagnetics. Appl. Phys. Rev. **4**, 021102 (2017)
25. M.A. Kats, F. Capasso, Optical absorbers based on strong interference in ultra-thin films. Laser Photon. Rev. **10**, 735 (2016)